



Continuous-zoom bifocal metasurfaces by mutual motion of cascaded bilayer metasurfaces in the visible

CHANG WANG,¹ YAN SUN,¹ QIANGBO ZHANG,¹ ZEQING YU,¹
CHENNING TAO,¹ JINLEI ZHANG,¹ FEI WU,² RENGMAO WU,¹ AND
ZHENRONG ZHENG^{1,*}

¹*State Key Lab of Modern Optical Instrumentation, Zhejiang University, Hangzhou 310058, China*

²*Beijing LLVision Technology Co., Ltd., Beijing 100000, China*

*zrz@zju.edu.cn

Abstract: Metasurfaces, a subcategory of metasurfaces, has been widely investigated by virtue of its miniature and ultrathin characteristics as well as versatile functionalities. In this study, a tunable bifocal metasurface with two continuous-zoom foci is proposed and numerically verified. This design utilizes two cascaded layers of metasurfaces, and different phase profiles for incidences of opposite helicities are imparted on each layer by the combination of geometric phase and propagation phase. When two layers of metasurfaces are actuated laterally, focal lengths of both foci are tuned continuously, with the difference of both focal lengths increasing or decreasing. Additionally, the zoom range for each focus can be designed at will, and the relative intensity of both foci can be modulated by altering the ellipticity of incidence, with the focusing efficiency of the bifocal metasurface varying from 19.8% to 32.7% for numerical apertures in a range from 0.53 to 0.78. The proposed device is anticipated to find applications in multi-plane imaging, optical tomography technique, optical data storage, and so on.

© 2021 Optical Society of America under the terms of the [OSA Open Access Publishing Agreement](#)

1. Introduction

Optical metasurfaces, arrays of subwavelength-spaced optical antennas at an interface, exhibit extraordinary capability of locally shifting the phase, amplitude and polarization state of the incident electromagnetic waves. Due to their versatility and effectiveness in wavefront shaping, metasurfaces have drawn extensive attention for a variety of applications such as anomalous refraction or reflection [1–9], metasurfaces [10–35], meta-hologram [36–39], generation of vortex beam [40–42], wave plates [43–45] and so forth. Among them, the ultrathin planar metasurfaces are of substantial interest because of its potential to replace conventional lenses which are bulky and achieve phase shift by gradual phase accumulation along the optical paths, and various types of metasurfaces with complicated functions were implemented, for instances, achromatic metasurfaces [15–17], dynamic metasurfaces [18–20], varifocal metasurfaces [21–27], multifocal metasurfaces [28–35] and other types of multi-functional metasurfaces.

Metasurfaces with multiple foci in longitudinal or transverse direction, called multifocal metasurfaces, plays a significant role in multi-plane imaging [28,46,47], optical data storage [48,49], optical tomography technology [50–52], micro-manipulating optics [33], polarization state detection [34], optical communications [32,53], and so on. By far, a group of multifocal metasurfaces have been reported, for example, space division multiplexing multifocal metasurfaces [28,33], bifocal metasurfaces achieving controllable relative intensity by combining geometric phase and propagation phase [29], bifocal metasurfaces with controllable relative intensity by adjusting the parameters of geometric phase elements in multilayer structure [30], helicity-multiplexed multifocal metasurfaces with different focal points under illumination of orthogonally polarized light [31,32,34], multifocal metasurfaces with working modes of transmission or reflection [35], etc. Focal lengths of the multiple

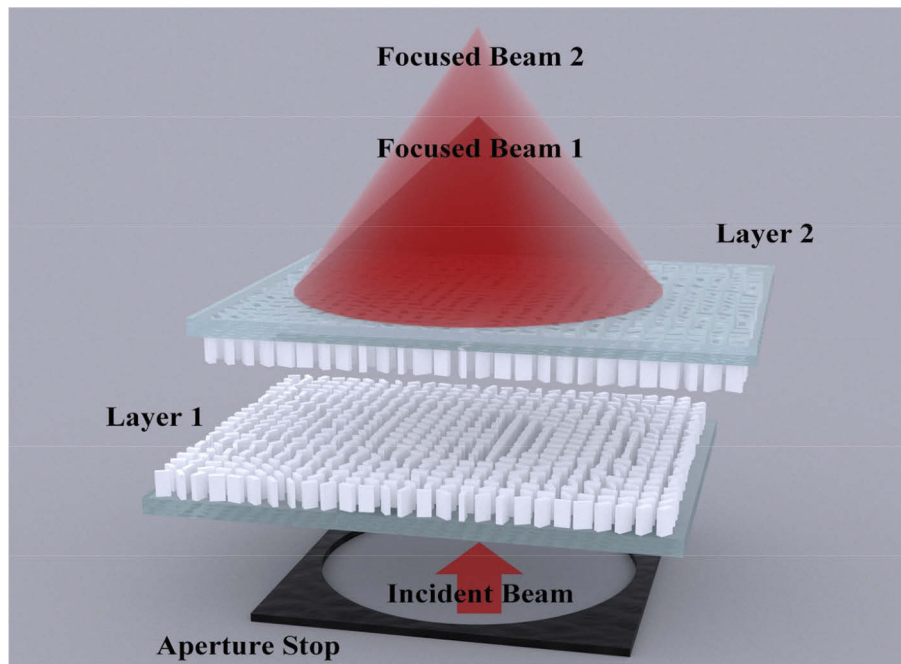


Fig. 1. Schematic representation of the TBML. The nanofins of both cascaded metasurface layers are arranged face to face with a small gap. An arbitrarily polarized plane wave passes through an aperture stop that is smaller than the working area of the TBML, and normally hits the device, generating two foci formed by the LCP and RCP components of the incidence. Both focal lengths are continuously tuned by the lateral actuation of both metasurface layers, and their relative intensity is modulated by the ellipticity of the incident light.

foci in these works are fixed after the corresponding designs are finalized, however, free control and continuous tunability of each focus formed by multifocal metalenses are of important use in realistic applications.

In this study, a tunable bifocal metalens (TBML) characterized with two continuous-zoom foci is proposed as shown in Fig. 1, with adjustable difference of focal lengths of both foci as well as their relative intensity. On the one hand, inspired by the Alvarez lens configuration [21,54,55], this design is composed of a bilayer of cascaded metasurfaces, made of face-to-face anisotropic titanium dioxide (TiO_2) nanofins on quartz substrates, and the phase manipulation is realized through combining the geometric phase and propagation phase [56], with each layer imparted with two distinct cubic polynomial phase distributions for left circular polarization (LCP) component and right circular polarization (RCP) component decomposed from the incidence, respectively. On the other hand, when two layers of metasurfaces are actuated laterally with a displacement, two changing quadratic polynomial phase profiles will be generated, thus producing two foci with different focal lengths along the longitudinal direction. The characteristics of the TBML are theoretically investigated and numerically verified by finite difference time domain (FDTD) method, and results illustrate that focal lengths of both two foci formed by LCP and RCP components of incidence are tuned continuously by the actuation, with one increasing and the other decreasing in a reconfigurable zoom range, while the difference of both focal lengths is also altered as long as it is larger than the minimum axial resolution. Furthermore, the TBML works as a polarization-insensitive metalens when both foci appear at the same position as a single focus, and at other situations the relative intensity of the two foci can be controlled by the ellipticity of the incidence, with the focusing efficiency of the TBML varying with the corresponding

numerical apertures (NA) that change from 0.53 to 0.78. This device is envisioned to find itself important applications in multi-plane imaging, optical tomography technique, optical data storage, optical communications and so on.

2. Theoretical analyses

The mechanism of optical phase discontinuities, derived from generalized laws of reflection and refraction [1], requires a converging phase compensation imparted on the metasurface interface. Normally the phase profile of a singlet metalens can either be of a hyperboloidal form [57], which results in a perfect spherical wavefront, or of a quadratic form [21,54], which can be utilized by Alvarez metasurfaces comprising two inverse cubic phase profiles as

$$\varphi_1(x, y) = -\varphi_2(x, y) = -A \left(\frac{1}{6}x^3 + \frac{1}{2}xy^2 \right), \quad (1)$$

where A is a positive and constant coefficient representing the rate of phase variation and (x, y) represents the horizontal position along metasurface planes in the Cartesian coordinates. Consider a bilayer of metasurfaces with two opposite cubic polynomial functions in Eq. (1), and when both layers are actuated laterally by a displacement d in opposite directions as shown in Fig. 2, the total phase of the Alvarez metasurface would be in a quadratic polynomial form as

$$\varphi_{\text{Alvarez}}(x, y) = \varphi_1(x + d, y) + \varphi_2(x - d, y) = -Ad(x^2 + y^2) - \frac{1}{3}Ad^3, \quad (2)$$

in the condition that the gap distance between two metasurface layers is small enough to avoid the deviation of φ_{Alvarez} from $\varphi_1 + \varphi_2$. Then, a tunable focal length inversely proportional to d will be generated as

$$f(d) = \frac{\pi}{\lambda Ad}, \quad (3)$$

after ignoring the constant phase term in Eq. (2) and comparing its quadratic term to the phase of a spherical singlet lens $\varphi_{\text{lens}}(x, y) = [\pi(x^2 + y^2)/(\lambda f)]$, where λ is the working wavelength and f is the focal length. This is how an Alvarez metasurface generates a focal spot with a tunable focal length, and focal spots at different positions will appear with their focal lengths tuned at the same time, provided that the total phase profile owns different coefficient values for different parts of the incident light. Thus, for a bifocal Alvarez metasurface with two different tunable focal spots, one feasible method is to decompose the incident light into components with orthogonal polarization states and impart both with different phase profiles.

Instead of using space division multiplexing strategies that have low efficiency as well as inflexible adjustment of relative intensity [29,35], the working mechanism of TBML combines geometric phase ψ and propagation phase η . It is known that geometric metasurfaces (GEMs) operate for circularly polarized light and impart opposite geometric phase distributions for LCP and RCP incidences by rotating nanostructures [56], while propagation phase is dependent on the geometric parameters of the nanostructures and insensitive to the polarization states of the incident light [29]. For instance, when a circularly polarized beam is incident on a nanostructure of GEMs, the transmitted light can be expressed as

$$E_t = \frac{t_L + t_S}{2} |\sigma\rangle + \frac{t_L - t_S}{2} \exp(i2\sigma\theta) |-\sigma\rangle, \quad (4)$$

where the spin-charge $\sigma = 1$ and $\sigma = -1$ represent LCP and RCP, respectively; $|\sigma\rangle = [1 + i\sigma]^T / 2^{1/2}$ is the unit vector of either CP; t_L and t_S are the complex coefficients for longer and shorter optical axes of the nanofin, θ is its rotation angle along z axis, and 2θ is equivalent to the geometric phase ψ . On the one hand, an ideal GEM nanostructure works as a half-wave plate, whose t_L should be

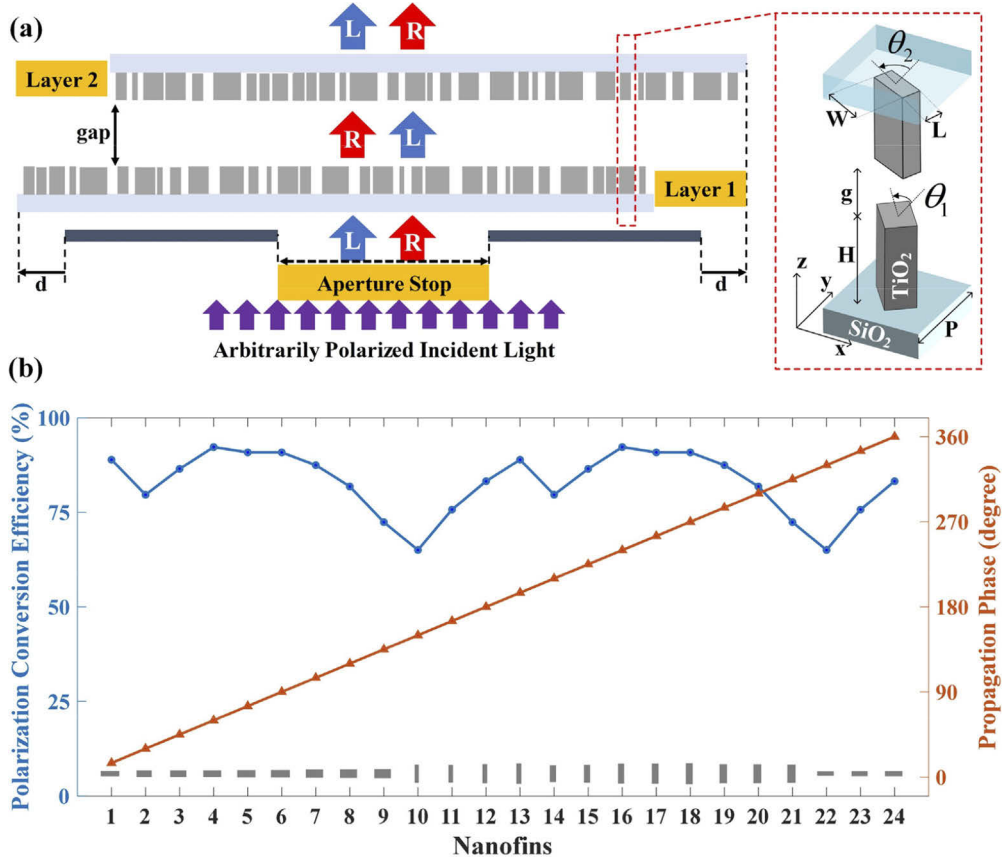


Fig. 2. (a) Schematic of the working principles. The TiO_2 nanofins on quartz substrates, with various rotating angles for generating geometric phases and diverse structural parameters for producing propagation phases at different positions on both metasurfaces layers, are spaced with a small gap distance. An arbitrarily polarized light normally hits first layer and is converted to a light with opposite helicity. After passing the second layer, the output light will be in the same polarization state as the incidence, and the total phase distributions are continuously changed when two layers are actuated laterally by a displacement d . (b) Polarization conversion efficiencies and the propagation phases of the 24-step nanofins simulated by the commercial package of Lumerical FDTD Solutions 2020 R2. The length and width parameters of unit cells from 1 to 24 are $L = 268, 220, 235, 262, 265, 274, 250, 247, 241, 60, 66, 69, 72, 90, 90, 96, 99, 108, 114, 120, 241, 232$ and 253 nm, and $W = 72, 90, 90, 90, 96, 99, 108, 114, 114, 120, 241, 232, 253, 268, 220, 235, 262, 265, 274, 250, 247, 241, 60, 66$ and 69 nm, respectively.

equal to $t_S \exp(i\pi) = -t_S$, making the first complex coefficient of Eq. (4), $(t_L + t_S)/2$, equal to zero; On the other hand, the second complex coefficient of Eq. (4), $(t_L - t_S)/2$, contains the propagation phase for the output with an orthogonal polarization state. Here, every single nanostructure of the TBML is assumed to have a very high PCE, so $(t_L + t_S)/2$ is regarded negligible, making Eq. (4) rewritten as

$$E_t = T \exp[i(\eta + 2\sigma\theta)] | -\sigma \rangle, \quad (5)$$

where the notation $T \cdot \exp(i\eta) = (t_L - t_S)/2$ is used for simplicity. Hence, for a metasurface with both phases imparted, the output phase distribution should be

$$\varphi_{\pm} = \eta \pm 2\theta = \eta \pm \psi, \quad (6)$$

where “+” and “-” represent LCP and RCP incident light, respectively, and φ_+ as well as φ_- can be chosen arbitrarily. In addition, Eq. (6) indicates that the geometric phase and the propagation phase could be expressed as $\psi = (\varphi_+ - \varphi_-)/2$ and $\eta = (\varphi_+ + \varphi_-)/2$, respectively. Furthermore, if the distance of both focal spots is required to be controlled for a tunable bifocal metalens, one solution is to increase the focal length for one focal spot while decrease that for the other when both metasurface layers are actuated. Moreover, it should be noted in Eq. (3) that when the relative displacement d values 0, the light would be focused at infinity, which does not satisfy practical requirements, so the varifocal ranges of both foci should be restricted within a certain scope. In this TBML design, the phase profiles of both layers, φ_1 and φ_2 , are creatively modified and reset as

$$\varphi_{1+}(x+d, y) = -A \left[\frac{1}{6}(x+d)^3 + \frac{1}{2}(x+d)y^2 \right] - \frac{1}{2}B[(x+d)^2 + y^2], \quad (7)$$

$$\varphi_{1-}(x+d, y) = A \left[\frac{1}{6}(x-l+d)^3 + \frac{1}{2}(x-l+d)y^2 \right] - \frac{1}{2}B[(x+d)^2 + y^2], \quad (8)$$

$$\varphi_{2+}(x-d, y) = -A \left[\frac{1}{6}(x+l-d)^3 + \frac{1}{2}(x+l-d)y^2 \right] - \frac{1}{2}B[(x-d)^2 + y^2], \quad (9)$$

and

$$\varphi_{2-}(x-d, y) = A \left[\frac{1}{6}(x-d)^3 + \frac{1}{2}(x-d)y^2 \right] - \frac{1}{2}B[(x-d)^2 + y^2], \quad (10)$$

where l is the changing range of d , and B is another positive and constant coefficient representing the rate of phase variation of the quadratic phase part added to the previous Alvarez phase profiles. Thus, the geometric phases and propagation phases of both layers can be described by $\psi_1 = (\varphi_{1+} - \varphi_{1-})/2$, $\eta_1 = (\varphi_{1+} + \varphi_{1-})/2$, $\psi_2 = (\varphi_{2+} - \varphi_{2-})/2$ and $\eta_2 = (\varphi_{2+} + \varphi_{2-})/2$.

When an LCP plane wave hits the first layer of the TBML, an output RCP light with a phase profile of φ_{1+} will be generated, and then it hits the second layer of the TBML, resulting in a final output of LCP light with a converging phase profile of $\varphi_{1+} + \varphi_{2-}$ as

$$\begin{aligned} \varphi_{\text{TBML+}}(x, y) &= \varphi_{1+}(x+d, y) + \varphi_{2-}(x-d, y) \\ &= -(Ad + B)(x^2 + y^2) - \frac{1}{3}Ad^3 - Bd^2. \end{aligned} \quad (11)$$

Similarly, when the TBML is hit by an RCP plane wave, the final output would be an RCP light with a converging phase profile of $\varphi_{1-} + \varphi_{2+}$ as

$$\begin{aligned} \varphi_{\text{TBML-}}(x, y) &= \varphi_{1-}(x+d, y) + \varphi_{2+}(x-d, y) \\ &= -[A(l-d) + B](x^2 + y^2) - \frac{1}{3}A(l-d)^3 - Bd^2. \end{aligned} \quad (12)$$

As a result, the focal lengths for LCP and RCP incidences are

$$f_+(d) = \frac{\pi}{\lambda(Ad + B)} \quad (13)$$

and

$$f_-(d) = \frac{\pi}{\lambda[A(l-d) + B]}, \quad (14)$$

respectively. Both foci have the same varifocal range, which changes from $\pi/[\lambda(Al + B)]$ to $\pi/(\lambda B)$. Special situations should be discussed according to Eqs. (13 and 14): for the case of

$d=0$, f_+ is maximized and f_- is minimized; for the case of $d=l$, f_+ is minimized and f_- is maximized; and for the case of $d=l/2$, both focal lengths equal $\pi/[\lambda(Al/2+B)]$, making the TBML a polarization-insensitive lens with a single focal spot. Additionally, when two foci do not superpose each other and they separate larger than a minimum axial resolution, the focal length difference would be

$$\Delta f = \frac{\pi}{\lambda(Ad+B)} - \frac{\pi}{\lambda[A(l-d)+B]}. \quad (15)$$

Another characteristic for utilizing geometric phase is that this TBML will become a helicity-multiplexed bifocal metasurface, and the relative intensities for both foci can be tuned by the ellipticity of the incident polarized light. Consider an arbitrarily polarized incident light, and its polarization state can be decomposed into two orthogonal circular polarization states by

$$E_i = \begin{bmatrix} E_x \\ E_y \end{bmatrix} = \frac{E_x - iE_y}{2} \begin{bmatrix} 1 \\ i \end{bmatrix} + \frac{E_x + iE_y}{2} \begin{bmatrix} 1 \\ -i \end{bmatrix}, \quad (16)$$

where E_i is the incident beam with arbitrary polarization; E_x and E_y are the linearly polarized components decomposed from E_i along x and y directions, respectively. For the case of $E_y = mE_x$ (m is a real number and $E_x \neq 0$) or $E_x = 0$, the incidence is linearly polarized (LP); for the case of $E_y = \pm iE_x$, the incidence is circularly polarized (CP, with “+” for LCP and “-” for RCP); in other cases, the incidence is elliptically polarized (EP). The notations $X = (E_x - iE_y)/2^{1/2}$, $Y = (E_x + iE_y)/2^{1/2}$, $L^{\sim} = [1, +i]^T/2^{1/2}$ and $R^{\sim} = [1, -i]^T/2^{1/2}$ are used to express Eq. (16) as $E_i = XL^{\sim} + YR^{\sim}$ for simplicity in the following explanations, while θ_1 and θ_2 denote the rotation angles of nanofins in the first and second layer. When E_i passes through the nanofins of the first layer, the transmitted electric field could be approximated by

$$E_{1t} = YT\exp[i(\eta_1 - 2\theta_1)]\tilde{L} + XT\exp[i(\eta_1 + 2\theta_1)]\tilde{R}. \quad (17)$$

Next, the incident electric field on the second layer, E_{2i} , is assumed to have no deviation from E_{1t} after passing through the gap that is small enough between two layers. The notation $T'\exp(i\eta') = (t'_L - t'_S)/2$ is used for the GEM nanostructure working as half-wave plates on the second layer, and the final transmitted field E_{2t} can be obtained as

$$\begin{aligned} E_{2t} &= XTT'\exp[i(\eta_1 + \eta_2 + 2\theta_1 - 2\theta_2)]\tilde{L} + YT'T'\exp[i(\eta_1 + \eta_2 - 2\theta_1 + 2\theta_2)]\tilde{R} \\ &= XTT'\exp[i(\eta_1 + \eta_2 + \psi_1 - \psi_2)]\tilde{L} + YT'T'\exp[i(\eta_1 + \eta_2 - \psi_1 + \psi_2)]\tilde{R} \\ &= XTT'\exp[i(\varphi_{1+} + \varphi_{2-})]\tilde{L} + YT'T'\exp[i(\varphi_{1-} + \varphi_{2+})]\tilde{R} \\ &= XTT'\exp[-i(Ad + B)(x^2 + y^2)]\tilde{L} + YT'T'\exp\{-i[A(l-d) + B](x^2 + y^2)\}\tilde{R}, \end{aligned} \quad (18)$$

which agrees well with Eq. (11) and Eq. (12). It is clear from Eq. (18) that the focusing intensities of both foci, which are formed by LCP and RCP light separately, can be modulated by the ellipticity of the arbitrarily polarized light.

3. Results and discussions

As is shown in Fig. 2(a), the TBML imparts orthogonal CP components, LCP and RCP, with different phase distributions by both metasurface layers, and thus focuses the collimated incident light into two different and tunable foci under transmission mode. The nanostructures of the TBML are constructed by high-aspect-ratio TiO₂ nanofins, with high refractive index and transmittance in the visible range [58], placed on quartz substrate as illustrated in the inset of Fig. 2. Then Fig. 3 shows the working mechanism of the nanofins demonstrated by Eqs. (7–10)

in two steps: for the first metasurface layer, different phase profiles, φ_{1+} and φ_{1-} , are separately imparted on LCP and RCP components from the incident light by opposite geometric phase $\pm\psi_1$ and same propagation phase η_1 ; for the second metasurface layer, the phase changes of φ_{2+} and φ_{2-} are also separately imparted on incidences with opposite helicity by opposite geometric phase $\pm\psi_2$ and same propagation phase η_2 . In addition, it is worth noting that although no anisotropic nanofin could work as a perfect half-wave plate according to the assumption in Eq. (5), the nanofins TiO_2 chosen in this TBML design should have high polarization conversion efficiencies (PCE), representing the proportion of the CP incidence that is converted to transmitted light with opposite helicity of polarization state. The parameter optimizations of the proposed nanofins as well as the following full wave simulations were performed using a FDTD 3D electromagnetic simulator from a commercial package of Ansys Lumerical 2020 R2 (Finite Difference IDE, 8. 24 version). As a result, the nanofin height H is set to be 600 nm, and the period of the unit cell P is set to be 300 nm to meet the Nyquist sampling criterion, which is $P < [\lambda/(1+NA_{\max})]$, at the design wavelength of 532 nm [59]. The optimized high PCE properties shown in Fig. 2(b) guarantee that the geometric phases, implemented via rotating nanofins with the rotation angles, will well cover the range from 0 to 2π . Meanwhile, the propagation phases determined by different nanofin length L and width W also cover the range from 0 to 2π , which is achieved by the 24-step unit cells with an incremental propagation phase of $\pi/12$ between adjacent nanofins.

For selecting an appropriate value of the gap distance g , half of Talbot distance that is equal to $2P^2/\lambda$ would be the optimal distance for superposing phases of two cascaded metasurfaces [60–62]. However, the Talbot distance in this case is 338 nm, which is not only likely to introduce non-negligible near-field effect but also too small for practical axial alignment in experimental setup. Here, 675 nm is selected as the value of the gap distance g , which is twice of the Talbot distance and a little larger than the incident wavelength of 532 nm, and this value is not too small for the above concerns but small enough for avoiding significant diffraction of the output wavefront generated by the first metasurface layer before it hits the second metasurface layer. In addition, to investigate the focusing characteristics, the designed zoom range of both foci generated by TBML varies from 12 μm ($\pi/[\lambda(Al+B)]$, Eq. (14)) to 24 μm ($\pi/(\lambda B)$, Eq. (13)) with an aperture determined by an aperture stop with the diameter of $D = 30 \mu\text{m}$, resulting in large numerical apertures (NA) in a range of 0.53 to 0.78 for both foci. For each metasurface layer, the area is set to be $30 \times 42 \mu\text{m}^2$ with 100 and 140 nanofins along x and y direction, respectively. Thus, the varying range l of the lateral displacement d of both layers is 6 μm as exhibited in Fig. 2 and Fig. 3, and the cubic polynomial phase variation coefficient A as well as the quadratic polynomial phase variation coefficient B are set to be 0.041 rad/ μm^3 and 0.246 rad/ μm^2 , respectively. In the following FDTD simulations, perfect matching layer (PML) boundary condition is applied at x -direction, y -direction and z -direction, and the simulated results of both foci with respect to varifocal performance, focal spot property, minimum focal length difference, focusing efficiency, relative intensities of both foci and other characteristics are discussed in section 3.1 and 3.2 below.

3.1. Characteristics of both continuous-zoom foci

Based on the theoretical analyses of Eqs. (11–14), the TBML works as a varifocal metalens with a single focal spot under the illuminated of pure LCP or RCP incidences. If no lateral displacement of both layers is actuated, which means $d = 0 \mu\text{m}$, the focal lengths of LCP incidence and RCP incidence, f_+ and f_- , are set to be 24 μm and 12 μm as designed. For this case, the intensity distributions of the TBML with $d = 0 \mu\text{m}$ in x - z plane are shown in Fig. 4. It can be seen from the simulated results in Fig. 4 and measured focal lengths in Fig. 6(a) that the simulated focal lengths of the TBML are 12.4 μm and 23.8 μm for RCP and LCP incidences, and remain the same values for both foci under LP incidence, agreeing well with the theoretical predictions. Moreover, as shown in Fig. 4(d-g), the FWHM describing the spot sizes of those foci are near

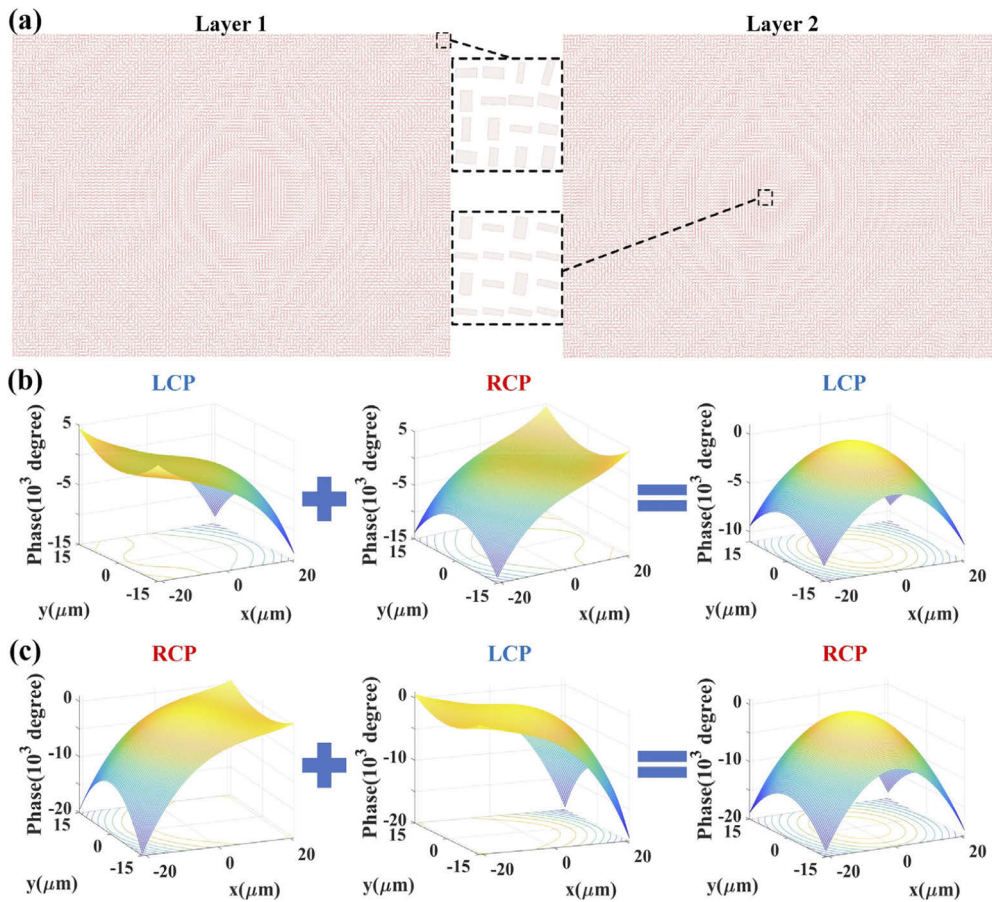


Fig. 3. (a) The top views of TiO_2 nanofins on both metasurface layers of the designed TBML. Nanofins at different positions have different cross sizes and rotation angles for generating various combinations of propagation phases and geometric phases. Three-dimensional phase profiles illustrating the phase manipulation mechanism: (b) the first layer imparts the LCP incidence with φ_{1+} and converts it to RCP, then the second layer imparts the RCP incidence with φ_{2-} , producing a total quadratic phase change of $\varphi_{\text{TBML}+} = \varphi_{1+} + \varphi_{2-}$ as the LCP focusing phase profile; (c) the second layer imparts the RCP incidence with φ_{1-} and converts it to LCP, then the second layer imparts the LCP incidence with φ_{2+} , producing a total quadratic phase change of $\varphi_{\text{TBML}-} = \varphi_{1-} + \varphi_{2+}$ as the RCP focusing phase profile;

diffraction limit, defined as working wavelength over twice of NA, thus the TBML has a good focusing performance and the difference of the focal spot sizes come from their different NAs. The FWHM of f_- under LP incidence is 450 nm and a little larger than that of f_+ under pure RCP incidence which is 423 nm, since the electric field near f_- is the result of superposition of both electric fields generated by LCP and RCP components, and the intensity value of the electric field below f_+ that is generated by LCP component cannot be ignored. It can be verified by Fig. 4 that the electric field intensity profile in Fig. 4(g) has more background noise than that in Fig. 4(e). On the contrary, the intensity value of the electric field above f_- that is generated by RCP component can be viewed negligible and would not affect the FWHM of f_+ under LP incident light. In addition, the focusing efficiencies, equal to the focusing power from a circular area with a diameter of three times of FWHM over the incident power, are 19.8% and 32.7% under RCP (12.4 μm as the smallest focal length) and LCP (23.8 μm as the largest focal length)

incidences. Furthermore, in order to investigate the continuous-zoom properties of the TBML, varifocal spots by different lateral displacements and various incidences are demonstrated by the intensity distributions in Fig. 5 and the measured focal length data from Fig. 6 (a and b) are analyzed in detail.

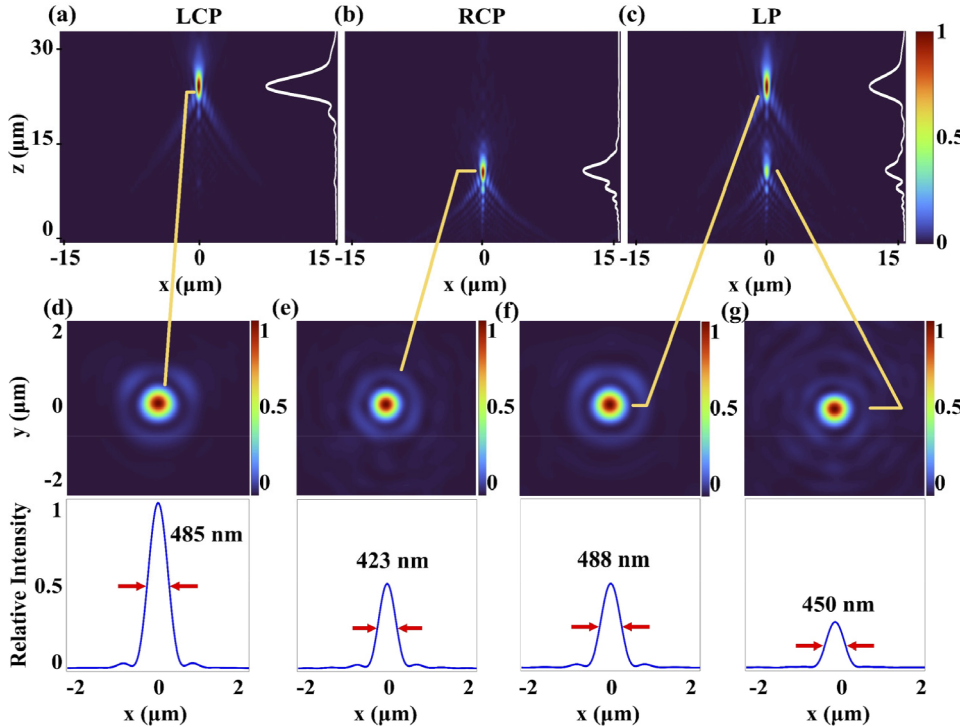


Fig. 4. The simulated results of TBML when $d = 0 \mu\text{m}$. (a-c) The intensity profiles of the transmitted electric field in x - z plane under LCP, RCP and LP incident light, respectively, with the corresponding intensity distributions along z axis represented by the white lines. (d) Simulated focal spot intensity profile under LCP incidence, with the full width at half-maximum (FWHM) of 485 nm for the corresponding horizontal cut. (e) Simulated focal spot intensity profile under RCP incidence, with the FWHM of 423 nm for the corresponding horizontal cut. (f and g) Simulated focal spots intensity profile formed by LCP and RCP components from the LP incidence, with the FWHM of 488 nm and 450 nm for the corresponding horizontal cuts.

It is clear in Fig. 5 that when increasing the displacement value d from 0 to 6 μm , the focal length of the focal spot formed by the LCP incidence decreases, from 23.8 to 12.4 μm as the simulated data in Fig. 6(a); the focal length of the focal spot formed by the RCP incidence increases, from 12.4 to 23.8 μm ; the focal length difference of both foci generated by LP incidence, which can be decomposed into LCP and RCP components, firstly decreases when d is increased from 0 to 2 μm , then go through a range of $2 \mu\text{m} < d < 4 \mu\text{m}$ as shown in Fig. 6(b) where both foci cannot be resolved since they are within the minimum axial resolution, and next increases when d is increased from 4 to 6 μm .

The symmetry properties in Fig. 5 imply that the focal length of the focus formed by LCP when d is chosen as a specific value d_0 , is equal to that of the focus formed by RCP when $d = l - d_0$; and the focal length difference of both foci is also of same value when the sum of two displacement values equal to l . These results meet the expectations of the working principles of

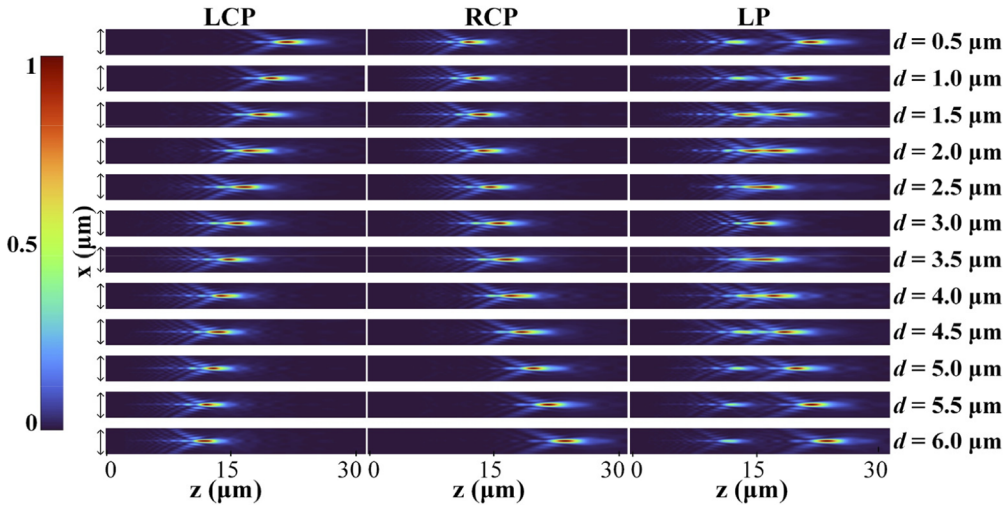


Fig. 5. The simulated electronic field intensity distributions of the varifocal performance of the TBML. Every subfigure has the same width, representing a dimension of $-2 \mu\text{m} < x < 2 \mu\text{m}$, and zooming of each focus is realized through laterally displacing both metasurface layers with respect to one another. The displacement d is changed from $0.5 \mu\text{m}$ to $6.0 \mu\text{m}$ with an increment of $0.5 \mu\text{m}$, under LCP, RCP and LP incidences, respectively.

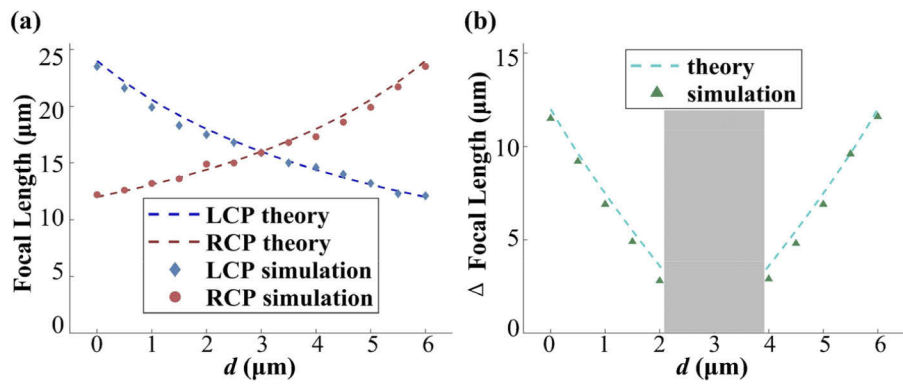


Fig. 6. (a) Theoretical and measured focal lengths of focal spot formed by pure LCP or RCP incidences. (b) Focal length difference values of both foci formed by LP or EP incidences, and the grey area represents a displacement range where both foci cannot be resolved.

TBML, and more importantly, the zoom range or varifocal limits of both foci can be designed at will according to Eqs. (13–15).

The results from Fig. 7(a-d) explore the axial resolution property of both foci under LP incidence. Figure 7(a and b) exhibit that the separate distance between two intensity peaks of both foci is 2.56 μm when $d = 2.0 \mu\text{m}$, and Fig. 7(c and d) show that the separate distance between two intensity peaks of both foci is 2.26 μm when $d = 2.1 \mu\text{m}$. In accordance with the axial resolution for $f_{\text{mid}} = 16 \mu\text{m}$ and $\text{NA}_{\text{mid}} = \sin[\tan^{-1}(D/2f_{\text{mid}})] = 0.684$, $d_{\text{ax}} = 2\lambda/\text{NA2 mid} = 2.275 \mu\text{m}$. Considering a minimum displacement increment $\Delta d = 0.1 \mu\text{m}$, $d = 2.1 \mu\text{m}$ is exactly the situation when both foci just cannot be resolved, and according to the symmetry property the unresolvable range is $d = 2.1 \sim 3.9 \mu\text{m}$. Thus, the minimum resolvable focal length difference is 2.56 μm when $d = 2.0$ or 4.0 μm , which accords well with the theoretical analyses above.

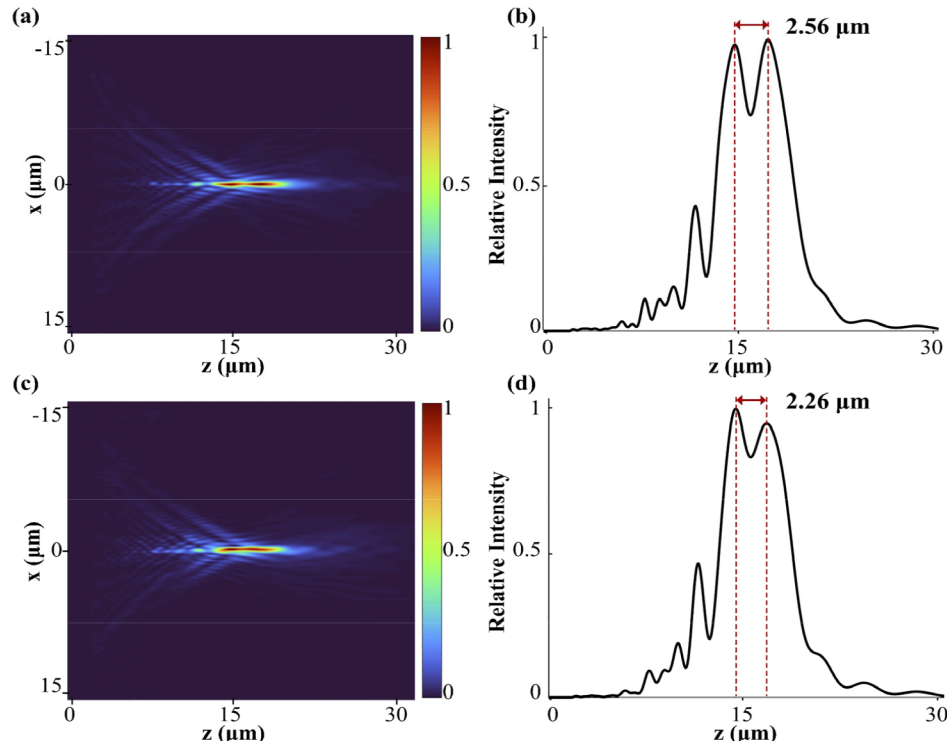


Fig. 7. (a and b) Electric field intensity distribution in x - z plane and intensity profile along z axis under LP incidence when $d = 2.0 \mu\text{m}$. (c and d) Electric field intensity distribution in x - z plane and intensity profile along z axis under LP incidence when $d = 2.1 \mu\text{m}$.

3.2. Relative intensities of both foci modulated by ellipticity of polarized incidence

The previous discussions focus on CP and LP incidences, while the incidence of an arbitrarily polarized incident could adjust the intensities of both foci. Based on Eq. (16), EP, which is an arbitrary polarization state besides CP and LP, could be decomposed into a pair of orthogonal polarization states, such as LCP and RCP. Further, according to Eqs. (17 and 18), the focusing intensities of both foci formed by the LCP and RCP components decomposed from the incident EP, are directly related to the complex decomposing coefficients of LCP and RCP, X and Y , respectively. Using the notation of $\tau = I_{\text{LCP}}/I_{\text{RCP}}$, where $I_{\text{LCP}}/I_{\text{RCP}}$ represents the relative intensity of LCP and RCP light decomposed from the EP incident light, the ellipticity of the EP incidence can be denoted as $\varepsilon = (1 - \tau^{1/2})/(1 + \tau^{1/2})$. It could be inferred that by adjusting the proportion

of ellipticity of the incident light, the relative intensity of both foci could be modulated as a result [29]. For example, it is an important situation for many bifocal imaging systems that equal intensities of both foci are required, and in Fig. 8(a, b, d and e), equal focusing intensities for both foci are realized through tuning the ellipticity of incidences with $\varepsilon = 0.22, 0.14, -0.14$ and -0.22 . These results are in good contrast with those in Fig. 5, where the relative intensities are clearly not equal under the incidences of LP light.

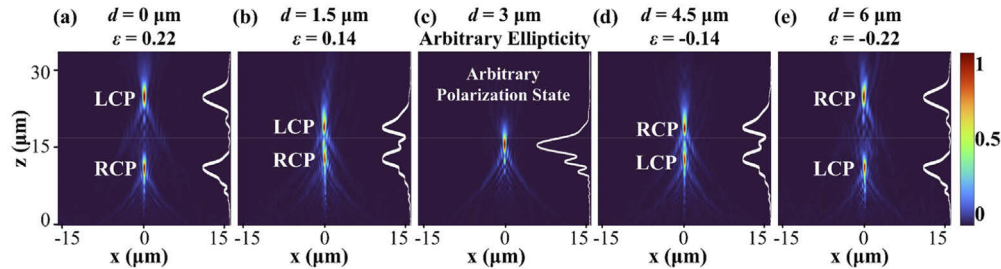


Fig. 8. (a, b, d and e) Under the incidences with the ellipticity of $\varepsilon = 0.22, 0.14, -0.14$ and -0.22 , the TBML has equal intensities for both foci for $d = 0, 1.5, 4.5, 6 \mu\text{m}$, respectively. (c) When $d = 3 \mu\text{m}$, both foci appear at the same position as $f_+ = f_- = 16 \mu\text{m}$, and the intensity as well as the focal length of the focal spot remain unchanged, regardless of the polarization state of incidence.

It is worth mentioning that both foci have same focal lengths of $16 \mu\text{m}$ when $d = 3 \mu\text{m}$ as shown in Fig. 6(a), and Fig. 8(c) illustrates that the intensity as well as the focal length of this focal spot remain unchanged, no matter what value of the ellipticity of the incident light is. In this special situation, the TBML works as a polarization-insensitive metalens with a single focal spot.

More simulations for different displacements and various ellipticities of incidences are carried out and demonstrated in Fig. 9, with the dashed-lines denoting the theoretically predicted values acquired by obtaining the equal-intensity points for each situation with various displacements. The simulated results agree well with the designed working principles of helicity multiplexing and the symmetry properties of the TBML focusing characteristics, proving the effectiveness of relative intensity tuning by changing the ellipticity of the arbitrarily polarized incident light.

Last but not least, it is worth discussing how the tunability as well as the implementation of this design could be achieved in practice, and the influencing factors in practical alignment should also be considered. Here, two kinds of experimental setups that can be used for characterizing both foci and testing the imaging properties of the bifocal metalens respectively are proposed and illustrated in Fig. 10 below. Above all, the TBML surely needs extremely precise translation stages to actuate the mutual motion of both metasurface layers, and each translation stage is expected to have a minimum motion resolution less than 50 nm for a zooming precision within $0.1 \mu\text{m}$ and maintaining the gap distance stable around twice of the Talbot distance as designed. As for the parallelism error, the difference of the maximum and minimum values of the gap distance g at layer edges can be assumed to be less than one Talbot distance, making the absolute value of the largest included angle, which is caused by such parallelism error, varies among an acceptable range from 0.46 degree to 0.64 degree. Besides, this error can be monitored by verifying whether both foci are along the desired optical axis, and this feedback information helps the high-resolution translation stages reduce the parallelism error. Additionally, there are numerous nanopositioning systems that could meet the above resolution requirements and work as the required translation stages. For instance, P-545.3R8S XYZ Piezo System from Physik Instrumente has a closed loop resolution of 1 nm and a travel range of $200 \mu\text{m}$ along three dimensions, and can be used in the proposed systems. Moreover, it should also be noted that a 532 nm laser with extremely narrow linewidth is supposed to be the monochromatic light

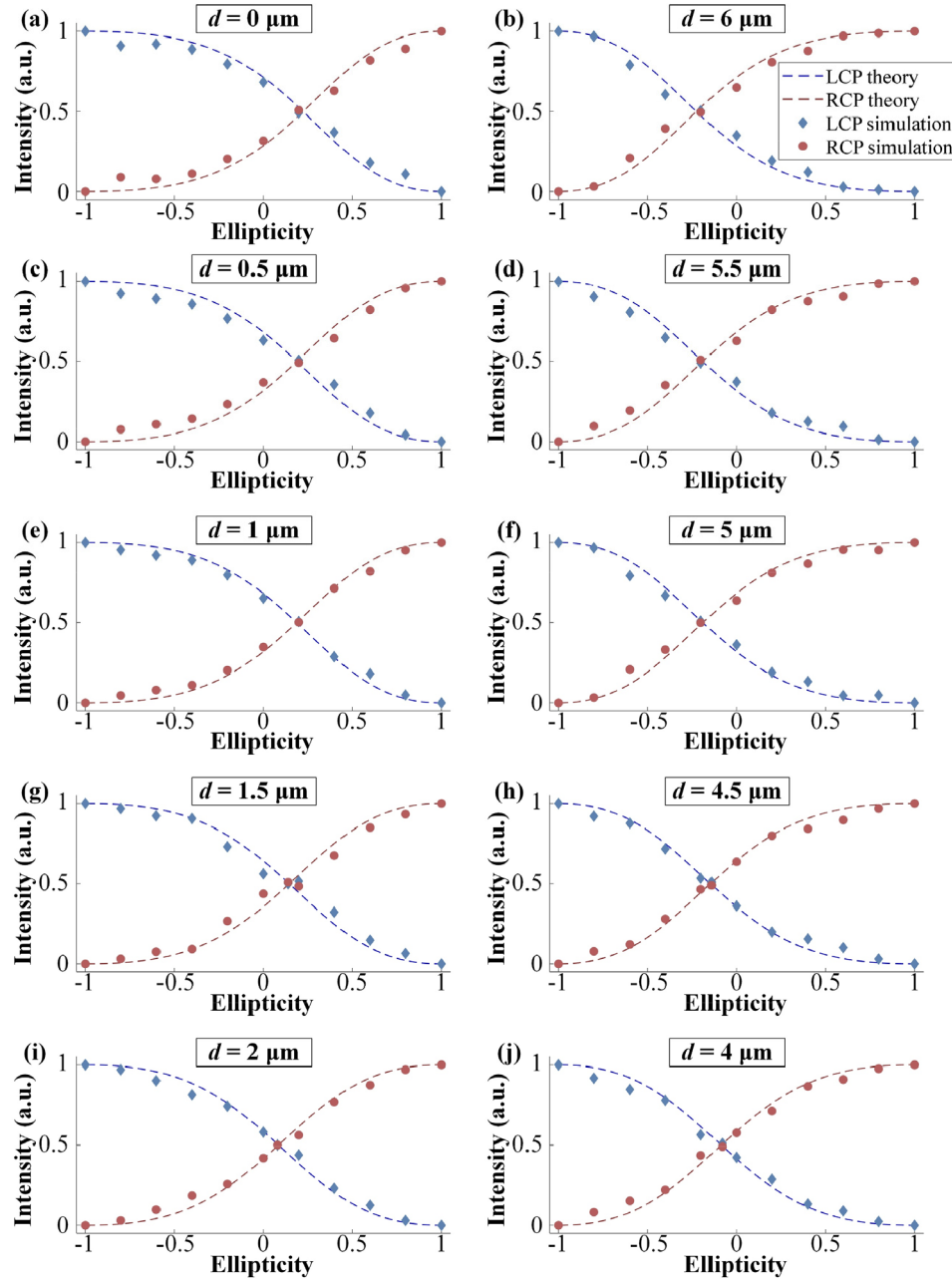


Fig. 9. Relative intensities of both foci when changing the ellipticity of the polarized incident light from -1 to 1 with an increment of 0.2 , under the situations that the actuated displacement of both metasurface layers is set as $d = 0, 0.5, 1.0, 1.5, 2.0, 4.0, 4.5, 5.0, 5.5, 6.0 \mu\text{m}$.

source, since the TBML is very sensitive to wavelength and the nanofin structural parameters are optimized for only 532 nm wavelength.

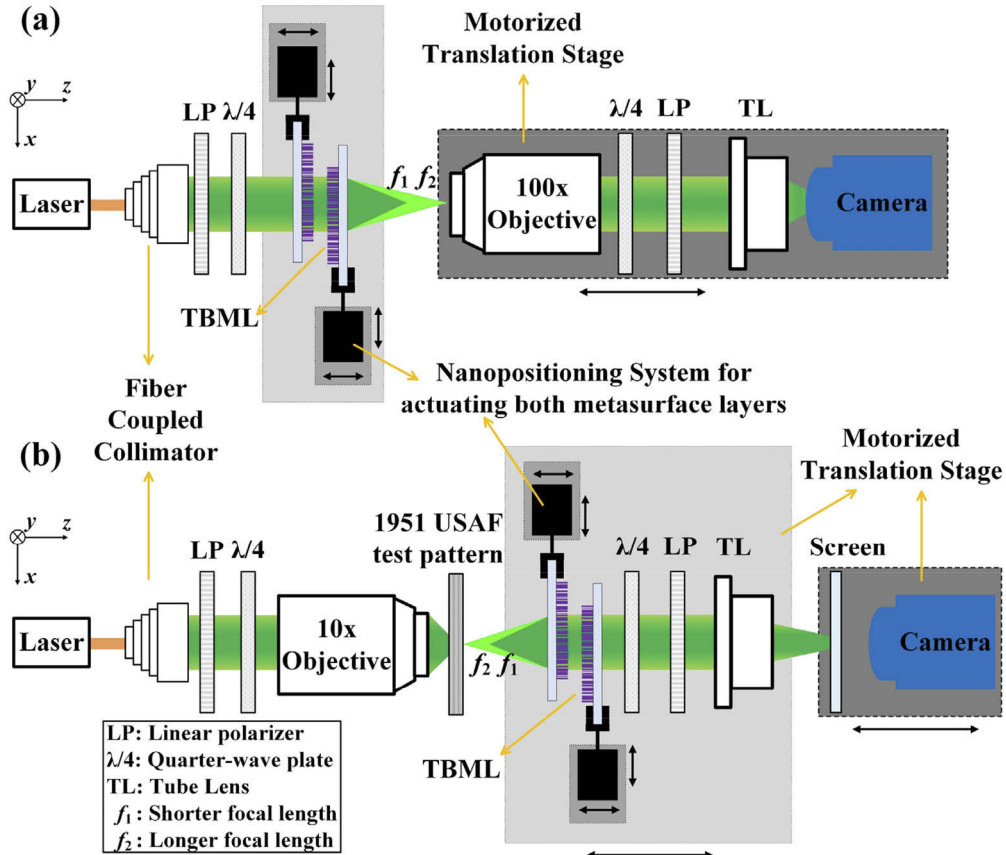


Fig. 10. (a) Schematic of the proposed experimental setup for characterizing both focal spots of the TBML. (b) Schematic of the proposed experimental setup for imaging with the TBML.

The first experimental setup as depicted in Fig. 10(a) is used for characterizing both foci of the TBML. A 532 nm laser beam is firstly collimated by a fiber collimator and then passes through a circular polarizer, composed of a linear polarizer as well as a quarter wave plate, for generating an elliptically polarized light, with its ellipticity being adjusted at will by relative rotation between the linear polarizer and the quarter wave plate. Next, the LCP and RCP components of the beam are separately focused by the TBML, with their focal lengths being tuned by actuating both nanopositioning systems laterally. An objective (100 \times magnification) is then used to capture, magnify and image both foci in order to analyze information like FWHM of the focal spots, with a tube lens behind it for forming the images on a camera. It is worth mentioning that another circular polarizer is placed between the objective and the tube lens in order to remove background noises, since it could be set as cross-polarized for only filtering LCP or RCP light and thus eliminating the undesired polarization components.

In the second experimental setup as shown in Fig. 10(b), a target object such as the 1951 USAF resolution test pattern is selected for characterizing the imaging properties of the TBML. After the laser beam being similarly collimated and made elliptically polarized, an objective (10 \times magnification) is utilized as a condenser for more intensive illumination on the resolution

target. Later, the TBML as well as the tube lens placed on a motion stage can work together as a microscopic imaging system, and the second circular polarizer placed between the objective and the tube lens is similarly used for removing undesired polarization components. In addition, the distance between the resolution target and the bifocal metalens could also be adjusted so that the image with full field of view is best focused and projected on a semi-transparent screen behind, preventing the image from being limited by the size of the camera sensor. Furthermore, it is also worth noting that the magnification of such microscopic imaging system can be changed by the varying focal lengths of both foci, and this system also achieves multi-plane imaging since it is helicity-multiplexed and both focal lengths of LCP and RCP light can be set as different values among the varifocal range.

4. Conclusions

In conclusion, a tunable bifocal metalens working in the visible band with two continuous-zoom foci, named TBML, is proposed. It is characterized by five aspects: firstly, both foci are generated by two cascaded layers of metasurfaces imparted by two specially designed Alvarez or cubic polynomial phases for LCP and RCP components of the polarized incident light, and when these two layers are actuated laterally for giving rise to two varying quadratic polynomial phases, two foci formed by LCP and RCP lights from the incidence will have tunable focal lengths that are different from each other; secondly, the phase manipulation is achieved through combining the geometric phase and propagation phase rather than space division multiplexing strategies, realizing good focusing efficiency for various numerical apertures of the bilayer configuration; thirdly, the phase distributions for both metasurface layers are realized with improved Alvarez phase profiles, making the zoom range reconfigurable at will and avoiding focusing at infinity, which is not practical; in addition, the difference of both focal lengths is controllable as long as it is larger than the minimum axial resolution; last but not least, since the TBML is polarization-sensitive, the relative intensity of both foci can also be effectively tuned by altering the ellipticity of the polarized incident light, along with a special working mode of polarization-insensitive metalens when both foci cover each other. The TBML provides previous bifocal metalenses with more freedoms of tunability, and it could be envisioned that this design may find potential applications in multi-plane imaging, optical data storage, optical tomography technique, optical communications, micro-manipulating optics, polarization state detection, etc.

Funding. National Natural Science Foundation of China (61327902); Beijing Municipal Science and Technology Commission (Z201100004020012).

Disclosures. The authors declare no conflicts of interest.

Data availability. Data underlying the results presented in this paper are not publicly available at this time but may be obtained from the authors upon reasonable request.

References

1. N. Yu, P. Genevet, M. A. Kats, F. Aieta, J.-P. Tetienne, F. Capasso, and Z. Gaburro, "Light propagation with phase discontinuities: generalized laws of reflection and refraction," *Science* **334**(6054), 333–337 (2011).
2. X. Ni, N. K. Emani, A. V. Kildishev, A. Boltasseva, and V. M. Shalaev, "Broadband light bending with plasmonic nanoantennas," *Science* **335**(6067), 427 (2012).
3. S. Sun, K.-Y. Yang, C.-M. Wang, T.-K. Juan, W. T. Chen, C. Y. Liao, Q. He, S. Xiao, W.-T. Kung, G.-Y. Guo, L. Zhou, and D. P. Tsai, "High efficiency broadband anomalous reflection by gradient metasurfaces," *Nano Lett.* **12**(12), 6223–6229 (2012).
4. M. Wei, Q. Xu, Q. Wang, X. Zhang, Y. Li, J. Gu, Z. Tian, X. Zhang, J. Han, and W. Zhang, "Broadband non-polarizing terahertz beam splitters with variable split ratio," *Appl. Phys. Lett.* **111**(7), 071101 (2017).
5. B. Wang, F. Dong, H. Feng, D. Yang, Z. Song, L. Xu, W. Chu, Q. Gong, and Y. Li, "Rochon-prism-like planar circularly polarized beam splitters based on dielectric metasurfaces," *ACS Photon.* **5**(5), 1660–1664 (2018).
6. D. Zhang, M. Ren, W. Wu, N. Gao, X. Yu, W. Cai, X. Zhang, and J. Xu, "Nanoscale beam splitters based on gradient metasurfaces," *Opt. Lett.* **43**(2), 267–270 (2018).
7. A. Ozer, N. Yilmaz, H. Kocer, and H. Kurt, "Polarization-insensitive beam splitters using all-dielectric phase gradient metasurfaces at visible wavelengths," *Opt. Lett.* **43**(18), 4350–4353 (2018).

8. H. Kocer, Y. Durna, H. Kurt, and E. Ozbay, "Dynamic beam splitter employing an all-dielectric metasurface based on an elastic substrate," *Opt. Lett.* **45**(13), 3521–3524 (2020).
9. C. Wang, S. Liu, Y. Sun, X. Tao, P. Sun, J. Zhang, C. Tao, R. Wu, F. Wu, and Z. Zheng, "Tunable beam splitter using bilayer geometric metasurfaces in the visible spectrum," *Opt. Express* **28**(19), 28672–28685 (2020).
10. M. Khorasaninejad, W. T. Chen, R. C. Devlin, J. Oh, A. Y. Zhu, and F. Capasso, "Metalenses at visible wavelengths: Diffraction-limited focusing and subwavelength resolution imaging," *Science* **352**(6290), 1190–1194 (2016).
11. A. Arbabi, Y. Horie, A. J. Ball, M. Bagheri, and A. Faraon, "Subwavelength-thick lenses with high numerical apertures and large efficiency based on high-contrast transmit arrays," *Nat Commun* **6**(1), 7069 (2015).
12. H. Zuo, D. Y. Choi, X. Gai, P. Ma, L. Xu, D. N. Neshev, B. Zhang, and B. Luther-Davies, "High-efficiency all-dielectric metalenses for mid-infrared imaging," *Adv. Opt. Mater.* **5**(23), 1700585 (2017).
13. J. Yuan, G. Yin, W. Jiang, W. Wu, and Y. Ma, "Design of mechanically robust metasurface lenses for RGB colors," *J. Opt.* **19**(10), 105002 (2017).
14. L. Lan, W. Jiang, and Y. Ma, "Three dimensional subwavelength focus by a near-field plate lens," *Appl. Phys. Lett.* **102**(23), 231119 (2013).
15. W. T. Chen, A. Y. Zhu, V. Sanjeev, M. Khorasaninejad, Z. Shi, E. Lee, and F. Capasso, "A broadband achromatic metalens for focusing and imaging in the visible," *Nat. Nanotechnol.* **13**(3), 220–226 (2018).
16. W. T. Chen, A. Y. Zhu, J. Sisler, Z. Bharwani, and F. Capasso, "A broadband achromatic polarization-insensitive metalens consisting of anisotropic nanostructures," *Nat Commun* **10**(1), 355 (2019).
17. S. Wang, P. C. Wu, V.-C. Su, Y.-C. Lai, C. Hung Chu, J.-W. Chen, S.-H. Lu, J. Chen, B. Xu, C.-H. Kuan, T. Li, S. Zhu, and D. P. Tsai, "Broadband achromatic optical metasurface devices," *Nat Commun* **8**(1), 187 (2017).
18. E. Arbabi, A. Arbabi, S. M. Kamali, Y. Horie, M. Faraji-Dana, and A. Faraon, "Mems-tunable dielectric metasurface lens," *Nat Commun* **9**(1), 812 (2018).
19. T. Roy, S. Zhang, I. W. Jung, M. Troccoli, F. Capasso, and D. Lopez, "Dynamic metasurface lens based on mems technology," *APL Photonics* **3**(2), 021302 (2018).
20. P. Ding, Y. Li, L. Shao, X. Tian, J. Wang, and C. Fan, "Graphene aperture-based metalens for dynamic focusing of terahertz waves," *Opt. Express* **26**(21), 28038–28050 (2018).
21. S. Colburn, A. Zhan, and A. Majumdar, "Varifocal zoom imaging with large area focal length adjustable metalenses," *Optica* **5**(7), 825–831 (2018).
22. C.-Y. Fan, T.-J. Chuang, K.-H. Wu, and G.-D. J. Su, "Electrically modulated varifocal metalens combined with twisted nematic liquid crystals," *Opt. Express* **28**(7), 10609–10617 (2020).
23. W. Liu, B. Hu, Z. Huang, H. Guan, H. Li, X. Wang, Y. Zhang, H. Yin, X. Xiong, J. Liu, and Y. Wang, "Graphene enabled electrically controlled terahertz meta-lens," *Photonics Res.* **6**(7), 703–708 (2018).
24. P. Gutruf, C. Zou, W. Withayachumnankul, M. Bhaskaran, S. Sriram, and C. Fumeaux, "Mechanically tunable dielectric resonator metasurfaces at visible frequencies," *ACS Nano* **10**(1), 133–141 (2016).
25. H.-S. Ee and R. Agarwal, "Tunable metasurface and flat optical zoom lens on a stretchable substrate," *Nano Lett.* **16**(4), 2818–2823 (2016).
26. A. She, S. Zhang, S. Shian, D. R. Clarke, and F. Capasso, "Adaptive metalenses with simultaneous electrical control of focal length, astigmatism, and shift," *Sci. Adv.* **4**(2), eaap9957 (2018).
27. Y. Cui, G. Zheng, M. Chen, Y. Zhang, Y. Yang, J. Tao, T. He, and Z. Li, "Reconfigurable continuous-zoom metalens in visible band," *Chin. Opt. Lett.* **17**(11), 111603 (2019).
28. X. Z. Chen, M. Chen, M. Q. Mehmood, D. Wen, F. Y. Yue, C. W. Qiu, and S. Zhang, "Longitudinal multifoci metalens for circularly polarized light," *Adv. Opt. Mater.* **3**(9), 1201–1206 (2015).
29. S. Tian, H. Guo, J. Hu, and S. Zhuang, "Dielectric longitudinal bifocal metalens with adjustable intensity and high focusing efficiency," *Opt. Express* **27**(2), 680–688 (2019).
30. R. Lin and X. Li, "Multifocal metalens based on multilayer pancharatnam berry phase elements architecture," *Opt. Lett.* **44**(11), 2819–2822 (2019).
31. T. Zhou, J. Du, Y. Liu, and X. Zang, "Helicity multiplexed terahertz multi-foci metalens," *Opt. Lett.* **45**(2), 463–466 (2020).
32. R. Ji, K. J. Chen, Y. J. Ni, Y. N. Hua, K.W. Long, and S. L. Zhuang, "Dual-focies metalens for co-polarized and cross-polarized transmission waves," *Advances in Condensed Matter Physics* **2018**, 2312694 (2018).
33. W. Wang, Z. Guo, K. Zhou, Y. Sun, F. Shen, Y. Li, S. Qu, and S. Liu, "Polarization-independent longitudinal multi-focusing metalens," *Opt. Express* **23**(23), 29855–29866 (2015).
34. R. Wang, J. Han, J. Liu, H. Tian, W. Sun, L. Li, and X. Chen, "Multi-foci metalens for terahertz polarization detection," *Opt. Lett.* **45**(13), 3506–3509 (2020).
35. L. Chen, Y. Hao, L. Zhao, R. Wu, Y. Liu, Z. Wei, N. Xu, Z. Li, and H. Liu, "Multifunctional metalens generation using bilayer all-dielectric metasurfaces," *Opt. Express* **29**(6), 9332–9345 (2021).
36. L. Li, T. J. Cui, W. Ji, S. Liu, J. Ding, X. Wan, Y. B. Li, M. Jiang, C.-W. Qiu, and S. Zhang, "Electromagnetic reprogrammable coding-metasurface holograms," *Nat Commun* **8**(1), 197 (2017).
37. G. Zheng, H. Mühlenbernd, M. Kenney, G. Li, T. Zentgraf, and S. Zhang, "Metasurface holograms reaching 80% efficiency," *Nat. Nanotechnol.* **10**(4), 308–312 (2015).
38. D. Wen, F. Yue, G. Li, G. Zheng, K. Chan, S. Chen, M. Chen, K. F. Li, P. W. H. Wong, and K. W. Cheah, "Helicity multiplexed broadband metasurface holograms," *Nat Commun* **6**(1), 8241 (2015).

39. Z.-L. Deng, J. Deng, X. Zhuang, S. Wang, T. Shi, G. P. Wang, Y. Wang, J. Xu, Y. Cao, and X. Wang, "Facile metagrating holograms with broadband and extreme angle tolerance," *Light Sci Appl* **7**(1), 78 (2018).
40. N. Shitrit, I. Bretner, Y. Gorodetski, V. Kleiner, and E. Hasman, "Optical spin Hall effects in plasmonic chains," *Nano Lett.* **11**(5), 2038–2042 (2011).
41. Y. Yang, W. Wang, P. Moitra, I. I. Kravchenko, D. P. Briggs, and J. Valentine, "Dielectric meta-reflect array for broadband linear polarization conversion and optical vortex generation," *Nano Lett.* **14**(3), 1394–1399 (2014).
42. P. Genevet, N. Yu, F. Aieta, J. Lin, M. A. Kats, R. Blanchard, M. O. Scully, Z. Gaburro, and F. Capasso, "Ultra-thin plasmonic optical vortex plate based on phase discontinuities," *Appl. Phys. Lett.* **100**(1), 013101 (2012).
43. H. Yang, G. Li, X. Su, G. Cao, Z. Zhao, F. Yu, X. Chen, and W. Lu, "Annihilating optical angular momentum and realizing a meta-waveplate with anomalous functionalities," *Opt. Express* **25**(15), 16907–16915 (2017).
44. Y. Zhao and A. Alù, "Tailoring the Dispersion of Plasmonic Nanorods To Realize Broadband Optical Meta-Waveplates," *Nano Lett.* **13**(3), 1086–1091 (2013).
45. J. Kim, S. Choudhury, C. DeVault, Y. Zhao, A. V. Kildishev, V. M. Shalaev, A. Alù, and A. Boltasseva, "Controlling the polarization state of light with plasmonic metal oxide metasurface," *ACS Nano* **10**(10), 9326–9333 (2016).
46. J. Hu, D. Wang, D. Bhowmik, T. Liu, S. Deng, M. P. Knudson, X. Ao, and T. W. Odom, "Lattice-resonance metalenses for fully reconfigurable imaging," *ACS Nano* **13**(4), 4613–4620 (2019).
47. M. Khorasaninejad, W. T. Chen, A. Y. Zhu, J. Oh, R. C. Devlin, D. Roussou, and F. Capasso, "Multispectral chiral imaging with a metalens," *Nano Lett.* **16**(7), 4595–4600 (2016).
48. S. Horiuchi, A. Fukumoto, and M. Yamamoto, "Analysis of crosstalk-free conditions for a cross-shift multiplexing method in holographic data recording," *Appl. Opt.* **57**(27), 7805–7810 (2018).
49. M. Salanga, B. Kersting, I. Ronneberger, V. P. Jonnalagadda, X. T. Vu, M. Le Gallo, I. Giannopoulos, O. Cojocaru-Mirédin, R. Mazzarello, and A. Sebastian, "Monatomic phase change memory," *Nat. Mater.* **17**(8), 681–685 (2018).
50. D. C. Adams and M. J. Suter, "Processing-based approach for resolving the sample optic axis in endoscopic polarization-sensitive optical coherence tomography," *Opt. Express* **26**(19), 24917–24927 (2018).
51. S. S. Tong, B. Han, and J. P. Tang, "Edge-guided TVp regularization for diffuse optical tomography based on radiative transport equation," *Inverse Probl.* **34**(11), 115009 (2018).
52. L.Y. Chen, M.C. Pan, and M.C. Pan, "Flexible near-infrared diffuse optical tomography with varied weighting functions of edge-preserving regularization," *Appl. Opt.* **52**(6), 1173–1182 (2013).
53. F. Zhang, M. B. Pu, J. Luo, H. L. Yu, and X. G. Luo, "Symmetry breaking of photonic spin-orbit interactions in metasurfaces," *Guangdian Gongcheng* **44**(3), 319–325 (2017).
54. I. M. Barton, S. N. Dixit, L. J. Summers, C. A. Thompson, K. Avicola, and J. Wilhelmsen, "Diffractive alvarez lens," *Opt. Lett.* **25**(1), 1–3 (2000).
55. Z. Du, B. Hu, W. Liu, J. Liu, and Y. Wang, "Tunable beam deflector by mutual motion of cascaded bilayer metasurfaces," *J. Opt.* **21**(11), 115101 (2019).
56. J. P. Balthasar Mueller, N. A. Rubin, R. C. Devlin, B. Groever, and F. Capasso, "Metasurface polarization optics: independent phase control of arbitrary orthogonal states of polarization," *Phys. Rev. Lett.* **118**(11), 113901 (2017).
57. F. Aieta, P. Genevet, M. A. Kats, N. Yu, R. Blanchard, Z. Gaburro, and F. Capasso, "Aberration-free ultrathin flat lenses and axicons at telecom wavelengths based on plasmonic metasurfaces," *Nano Lett.* **12**(9), 4932–4936 (2012).
58. T. Siefke, S. Kroker, K. Pfeiffer, O. Puffky, K. Dietrich, D. Franta, I. Ohlidal, A. Szeghalmi, E. B. Kley, and A. Tunnermann, "Materials pushing the application limits of wire grid polarizers further into the deep ultraviolet spectral range," *Adv. Opt. Mater.* **4**(11), 1780–1786 (2016).
59. S. M. Kamali, E. Arbabi, A. Arbabi, Y. Horie, and A. Faraon, "Highly tunable elastic dielectric metasurface lenses," *Laser Photonics Rev.* **10**(6), 1002–1008 (2016).
60. S. Bernet and M. Ritsch-Marte, "Adjustable refractive power from diffractive Moiré elements," *Appl. Opt.* **47**(21), 3722–3730 (2008).
61. S. Bernet, W. Harm, and M. Ritsch-Marte, "Demonstration of focus-tunable diffractive moiré-lenses," *Opt. Express* **21**(6), 6955–6966 (2013).
62. N. Yilmaz, A. Ozdemir, A. Ozer, and H. Kurt, "Rotationally tunable polarization-insensitive single and multifocal metasurface," *J. Opt.* **21**(4), 045105 (2019).